Quarterly Journal of the Royal Meteorological Society
A journal of the atmospheric sciences and physical oceanography

RMetS
Royal Meteorological Society

The influence of resolved convective motions on scalar dispersion in hectometric scale numerical weather prediction models

SCHOLARONE™
Manuscripts

The influence of resolved convective motions on scalar dispersion in hectometric scale numerical weather prediction models

Lewis P. Blunn[1,2,3*] | Robert S. Plant[2] | Omduth Coceal[2,3†] | Sylvia I. Bohnenstengel[1] | Humphrey W. Lean[1] | Janet F. Barlow[2]

[1]MetOffice@Reading, University of Reading, Reading, RG6 6ET, UK

[2]Department of Meteorology, University of Reading, Reading, RG6 6ET, UK

[3]National Centre for Atmospheric Science (NCAS), University of Reading, Reading, RG6 6ET, UK

Correspondence
Department of Meteorology, University of Reading, Reading, RG6 6ET, UK
Email: r.s.plant@reading.ac.uk

Present address
[*]MetOffice@Reading, University of Reading, Reading RG6 6ET, UK
[†]Department of Meteorology, University of Reading, Reading, RG6 6ET, UK

The UK Met Office has a 300 m grid length numerical weather prediction (NWP) model running routinely over London and in research mode city-scale hectometric grid length NWP has become commonplace. It is important to understand how moving from kilometre to hectometre scale grid length NWP influences boundary layer vertical mixing. For a clear-sky convective boundary layer (CBL) case study, using 55 m and 100 m grid length NWP, we demonstrate that CBL vertical mixing of passive scalar is almost fully resolved. Passive scalar converges near the surface after emission from an idealised pollution ground source representing city-scale emissions, and is transported in updrafts preferentially into the upper boundary layer. Approximately 8 km downstream of the source edge this causes 34% lower near-surface concentrations compared to 1.5 km grid length NWP, where vertical mixing is fully parameterised. This demonstrates that resolving ballistic type dispersion, which is not typically represented in NWP vertical mixing parameterisations, can have a leading order influence on city-scale near-surface pollution concentration. We present a simple analytical model that is able to capture diffusive and ballistic dispersion behaviour in terms of effective timescales. The timescale con-

trolling how long it takes passive scalar to become well-mixed in the CBL is ≈ 3 times longer for the 1.5 km compared to the 100 m and 55 m grid length NWP.

KEYWORDS

hectometric, air quality, dispersion, lagrangian stochastic model, city-scale

1 | INTRODUCTION

Over the past decade several studies have evaluated kilometre versus sub-kilometre scale numerical weather prediction (NWP) for different meteorological applications (Hagelin et al., 2014; Leroyer et al., 2014; Hanley et al., 2015; Boutle et al., 2016; Hanley et al., 2016; Ronda et al., 2017; Belair et al., 2018; Leroyer et al., 2022). At sub-kilometre horizontal grid lengths (Δ) urban areas are better represented in NWP, and therefore these models are often referred to as "urban-scale". For $\Delta = O(100m)$, unlike $\Delta = O(1km)$, the majority of convective boundary layer (CBL) turbulence is explicitly resolved (Boutle et al., 2014; Honnert et al., 2020), and turbulent structures such as horizontal convective rolls (HCRs) are simulated (Lean et al., 2019). Until now, the influence of parameterising ($\Delta \geq O(1km)$) versus explicitly resolving CBL vertical mixing of passive scalars in NWP has not been investigated. This study assesses the potential improvements and changes in vertical mixing behaviour when moving from $\Delta = O(1km)$ to $\Delta = O(100m)$ NWP.

Turbulent dispersion of particles has two different behaviours at long and short times after release. In the long time "diffusive" limit, defined as times greater than the order of a decorrelation timescale τ, dispersion is less efficient, since particles have lost memory of the initial eddy into which they were released. The particles undergo random motion, with the mean square displacement of particles increasing proportional to time (Taylor, 1922). In the short time "ballistic" limit, particles travel at the velocity within the eddy they were released into, and the mean square displacement of particles increases proportional to the time squared (Taylor, 1922). First using large-eddy simulation (LES) (Deardorff, 1972b), then experimentally using a water convection chamber (Willis and Deardorff, 1976), it was found that ballistic type dispersion results in passive scalar having a "lift-off" behaviour when released near the surface. At times on the order of a convective eddy turnover time (t_*) (Lilly, 1968; Deardorff, 1970), particles have a larger likelihood of being in the upper than lower half of the CBL, and there is a decrease in near-surface concentration.

Passive scalar dispersion in NWP can be used to understand aspects of pollution dispersion in air quality models (AQMs), since chemical species in AQMs are treated as passive scalars when transported (Warhaft, 2000; Kukkonen et al., 2012; Baklanov et al., 2014). Also, like NWP, regional to global scale AQMs generally use K-theory (sometimes with an additional counter-gradient term) to parameterise turbulent mixing (Kukkonen et al., 2012; Baklanov et al., 2014), so results from NWP are applicable to AQMs. City-scale AQMs that resolve urban topography typically use advanced Gaussian plume dispersion models (McHugh et al., 1997; Cimorelli et al., 2005; Stockie, 2011), which, like K-theory based dispersion models, only represent diffusive type dispersion. Exceptions to the rule are Lagrangian stochastic models (LSMs) (Wilson and Sawford, 1996; Thomson and Wilson, 2012) (such as the UK Met Office's NAME Model (Webster and Thomson, 2018)) which can incorporate ballistic type dispersion.

Here, for the first time it is possible to evaluate city-scale CBL vertical mixing of passive scalar at $\Delta = O(1km)$ and $\Delta = O(100m)$ within one NWP framework (the UK Met Office Unified Model (MetUM)), enabling investigation of the implications for AQMs when ballistic type dispersion is represented. Previous studies employing methods capable of representing both diffusive and ballistic dispersion have been for point sources or distributed sources, with study

regions of limited streamwise extent. The size restriction is caused by computational cost (LES) or limited chamber size (experiments) (Deardorff, 1972b; Willis and Deardorff, 1976, 1981; Gopalakrishnan and Avissar, 2000; Dosio et al., 2003, 2005). Previous literature has therefore not explored the full city-scale downstream evolution of passive scalar from a city-scale ground source.

We study vertical mixing of continuous and puff released passive scalar from a homogeneous ground-area source for a clear-sky CBL case study (4th May 2016) at $\Delta = 55$ m, $\Delta = 100$ m, and $\Delta = 1.5$ km. The idealised pollution emissions (i.e., passive scalar) are transported by NWP simulations that have fully realistic meteorology. Our research questions are:

- Is the three-dimensional spatial structure and evolution of the passive scalar field realistic in $\Delta = O(100m)$ NWP?
- Can a reduced analytical model capture timescales that characterise the different vertical mixing regimes in $\Delta = O(1km)$ and $\Delta = O(100m)$ NWP?
- Does resolving ballistic type dispersion affect city-scale evolution of near-surface pollution concentration?

The paper is structured as follows: Sect. 2 describes the case study, MetUM configurations, and passive scalar sources, Sects. 3.1.1 and 3.1.2 analyse the CBL and passive scalar field structure in the vertical and horizontal, respectively, Sect. 3.2 qualitatively interprets the vertical mixing dynamics, Sect. 3.3 quantifies the vertical mixing behaviour with timescales from a reduced analytical model, Sect. 3.4 investigates the importance of ballistic type dispersion on city-scale near-surface concentrations, Sect. 4 summarises and discusses the paper findings, and Appendix 1 outlines the reduced analytical model.

2 | METHODS

2.1 | Case Study

The chosen case study date is 4th May 2016. South-East England was under a high pressure system centred on continental Europe (Blunn, 2021). According to the London Urban Meteorological Observatory (LUMO; Kotthaus and Grimmond (2014)) it was a clear-sky day. This is based on the definition that at least 3 of the 4 ceilometers had no overhead cloud at any height more than 99% of the time. A clear-sky day was chosen since clear-sky conditions are conducive to strong CBL mixing. Also, they are the most simple conditions in which to study CBL mixing, since there is no influence from cloud generated latent heating or turbulence.

At University of Reading Atmospheric Observatory (URAO, ≈ 60 km west of Central London, 51.44 °N 0.94 °W, blue cross Fig. 1a) the hourly-average 10 m wind direction was predominantly from the south between 08:00 UTC and 22:00 UTC, varying between 165° and 203°, with a mean of 186°. Sensible heat flux (Q_H) observations were available from a network of three scintillometers separated by $1 - 3$ km in Central London (Crawford et al., 2017). Between 11:00 UTC and 15:00 UTC, hourly averaged Q_H was $300 - 400$ W m^{-2} for the different scintillometer paths. At URAO the average 10 m wind speed was 2.8 m s^{-1} during the same period. Given the moderate wind speeds and large Q_H, the case date is suitable for the study of an archetypal CBL. The aim of this study is not an evaluation of the modelled convection as Doppler lidar observations are not available unlike in Lean et al. (2019).

2.2 | Model Configuration

The MetUM (version 10.5) simulations are performed using a one-way nested research suite centred on London. See Table 1 and Fig. 1a for the model configurations and domains, respectively. The simulations contain idealised passive

scalar emissions (see Sect. 2.3), but fully realistic meteorology (e.g., microphysics, orography, and land—atmosphere exchanges). The outermost nest is the variable resolution UKV model (Tang et al., 2013) which has $\Delta = 1.5$ km over South-East England. Archived operational UKV model output are used to provide initialisation and hourly lateral boundary conditions (LBCs). The UKV nest provides LBCs to the $\Delta = 500$ m model (UM500), which passes LBCs to the $\Delta = 300$ m model (UM300), which finally passes LBCs to drive both the $\Delta = 100$ m (UM100) and $\Delta = 55$ m (UM55) models. LBCs for the 500–55 m models have a frequency of 15 min. The simulation start times are 00:00 UTC for the UKV and UM500, 03:00 UTC for the UM300, and 06:00 UTC for the UM100 and UM55, so that the time period common to all models is 06:00–22:00 UTC, allowing at least 5 hours for the turbulence to spin up in all of the models before first model output analysis (11:00 UTC).

TABLE 1 Model configurations.

Model	Horizontal Grid Length	Domain size (grid points)	Time step	Vertical levels
UKV	1.5 km	744 × 928	60 s	70
UM500	500 m	600 × 600	10 s	140
UM300	300 m	430 × 430	10 s	140
UM100	100 m	800 × 800	3 s	140
UM55	55 m	1440 × 1440	2 s	140

Lean et al. (2019) used an almost identical UM nesting suite and tested a $\Delta = 100$ m model domain with 30 km × 30 km horizontal extent. Turbulence did not "spin up" until $10 - 15$ km downstream of the inflow boundary. By extending the horizontal extent of the domain to 80 km × 80 km the turbulence had fully developed before it reached the London area (approximately 50 km × 50 km). The case study was clear-sky CBL like the one presented here, so the same 80 km × 80 km domain has been used for the 100 m and 55 m models. The domain top in all models is at 40 km. A Charney-Phillips vertical grid is used where there are half levels (containing e.g., horizontal velocities and pressure) that are staggered with full levels (containing e.g., potential temperature, passive scalar, and vertical velocity). Spacing is quadratic so that there is higher vertical resolution within the BL than above. The UKV uses a 70 vertical level set which has 23 full levels within the lowest 2 km at heights 5.0, 21.7, 45.0, and 75.0 m within the lowest 100 m, and the other models use a 140 vertical level set which has 52 full levels within the lowest 2 km at heights 2.0, 5.3, 10.0, 16.0, 23.3, 32.0, 42.0, 53.3, 66.0, 80.0, and 95.3 m within the lowest 100 m.

The MetUM version 10.5 dynamical core ("ENDGame") solves fully compressible, non-hydrostatic, deep-atmosphere dynamics using a semi-implicit semi-Lagrangian (SISL) numerical scheme (Davies et al., 2005; Wood et al., 2014). The scale-aware blended boundary layer (BL) scheme is used for sub-grid turbulent mixing (Boutle et al., 2014). With decreasing Δ more turbulence is resolved, and the blending is increasingly weighted towards the local three-dimensional (3D) Smagorinsky-Lilly turbulence scheme (Lilly, 1962; Smagorinsky, 1963; Halliwell, 2017) rather than the non-local one-dimensional (1D) BL scheme (Lock et al., 2000). The land surface model is the Joint UK Land Environment Simulator JULES (Best et al., 2011; Clark et al., 2011) and the module MORUSES treats the urban aspects of the surface (Porson et al., 2010; Bohnenstengel et al., 2011). MORUSES parametrises interactions between the urban surface and the atmosphere by assuming a 2D infinite street canyon geometry that accounts for the height and separation of buildings.

Analysis focuses on the UKV, UM100, and UM55 because of scalar non-conservation issues in the UM500 and UM300. At $\Delta = O(500\text{m})$ the dominant CBL turbulence is in the "grey zone" (Wyngaard, 2004; Honnert et al., 2020),
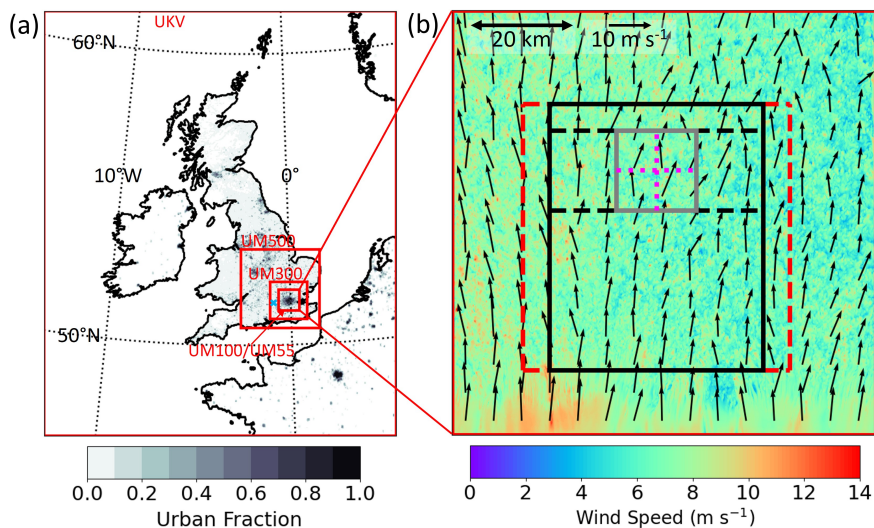
FIGURE 1　(a) Nesting suite schematic with urban fraction plotted. Each nest is highlighted in red. The outermost nest is the UKV, and in decreasing domain size order the other nests are the UM500, UM300, UM100, and UM55. The UM100 and UM55 have the same domain size. URAO is highlighted with a blue cross and is just to the west of the UM100/UM55 domain. (b) UM55 wind speed map at 13:00 UTC at height 300 m. The arrows are wind vectors. Highlighted are the puff release ground source area (red solid line, around the full region displayed in (b)), continuous release ground source area (red dashed line), analysis region 1 (black dashed line), analysis region 2 (black solid line), horizontal cross-section location (grey solid line) (Fig. 4), west-east vertical cross-section location (horizontal magenta dotted line) (Fig. 3), and south-north vertical cross-section location (vertical magenta dotted line) (Fig. 6).

and updrafts become grid scale. Also, SISL advection is not inherently conserving, meaning that when wind is interpolated from grid points straddling a departure point in a single grid point updraft, there is cancellation of the wind, resulting in insufficient scalar dilution in the updraft, and excess scalar is produced (Blunn, 2021). The UKV, UM100, and UM55 passive scalar is much less influenced by the passive scalar non-conservation issues, because the updrafts are not grid-scale in the mixed layer of the CBL. Also, the excess passive scalar produced in the UM500 and UM300 does not influence the other models, because the passive scalar is not passed between model boundaries. There is ongoing work at the UK Met Office on ameliorating scalar non-conservation issues.

2.3 | Source and Analysis Regions

Two passive scalars are included in the simulations, one with continuous and the other with puff release from a ground area source. The same source areas and emission rates are used in all models to facilitate comparison. The continuous release passive scalar is from a homogeneous ground source with horizontal dimensions 50 km × 50 km (red dashed line, Fig. 1b). The source provides a simple framework in which to study idealised city-scale spatial variation of passive scalar concentration over London. The puff release passive scalar is also from a homogeneous ground source, but with its horizontal extent covering the entire UM100/UM55 domains (red solid line, Fig. 1b). The puff releases are used to analyse vertical mixing timescales. On the hour passive scalar is released and at the end of the hour it is completely flushed from the domain. An hour is long enough for the passive scalar to become well-mixed in the CBL. The large

source area enables an analysis region to be selected far enough in from the source boundaries that zero passive scalar air is not advected in within the hour.

Analysis region 1 (black dashed line, Fig. 1b) starts 30 km downstream of the southern edge of the continuous source, extends 15 km downstream, and is 40 km in the cross-stream. It is large enough to contain > 10 CBL eddies (each with size of O(1 km)), has minimal flow variation (~ 1 m s^{-1}, Fig. 1b) on the scale of the analysis region, and has minimal z_i variation ($< 5\%$) on the scale of the analysis region. This ensures that flow statistics are robust and locally representative. Analysis region 2 (black solid line, Fig. 1b) is used to study the evolution of the vertical passive scalar distribution with downstream distance from the upstream edge of the continuous release source (Sect. 3.4).

3 | RESULTS AND DISCUSSION

3.1 | Convective Boundary Layer Structure

In this section, the vertical (Sect. 3.1.1) and horizontal (Sect. 3.1.2) structure of the CBL is analysed. Vertical profiles and vertical cross-sections provide information on the general structure of the CBL during the case study, and insights into vertical-mixing and passive scalar distribution differences between model resolutions. Passive scalar horizontal cross-sections and vertical velocity two-point correlations further elucidate these differences.

3.1.1 | Vertical Structure

Vertical profiles of several variables are calculated within analysis region 1 (Fig. 1b) at 13:00 UTC for the continuous release passive scalar and are plotted in Fig. 2. Height from the ground z on the y-axis is normalised by $\langle z_i \rangle$, where z_i is the boundary layer height, horizontally-averaged $\langle \rangle$ within analysis region 1. Concentrations are normalised by the average concentration in the BL, c_{BL}. z_i is diagnosed by performing an adiabatic parcel ascent until the parcel becomes negatively buoyant.

The UM100 and UM55 passive scalar concentration c (Fig. 2a) decreases sharply in the surface layer ($z/\langle z_i \rangle \approx 0.0 - 0.1$), is approximately constant in the mixed layer ($z/\langle z_i \rangle \approx 0.1 - 0.8$), before decreasing through the capping inversion layer ($z/\langle z_i \rangle \approx 0.8 - 1.2$) to zero. Similar behaviour can be seen for the UM100 and UM55 potential temperature θ in Fig. 2b, except that θ increases in the capping inversion layer. The UM100 and UM55 passive scalar and potential temperature profiles exhibit classic CBL structure (Garratt, 1994; Pleim, 2007).

The UKV c (Fig. 2a) and θ (Fig. 2b) vary more strongly with height in the mixed-layer compared to the UM100/UM55. The capping inversion is narrower for the UKV, and there is less passive scalar concentration above $\langle z_i \rangle$. This is because the UM100 and UM55 have greater z_i heterogeneity due to updrafts and downdrafts. Also, resolved motions in the UM100 and UM55 sometimes generate low θ anomalies in the middle of the CBL, leading to erroneously low parcel ascent z_i diagnosis (see Fig. 3c), and low θ and high c above z_i.

The UM100 and UM55 wind speeds are very similar (Fig. 2c) and are ≈ 6 m s^{-1} between $z/\langle z_i \rangle \approx 0.1 - 1.2$. The UKV wind speed has a maximum wind speed of 7.8 m s^{-1} at $z/\langle z_i \rangle \approx 0.2$ and decreases to similar values (≈ 6 m s^{-1}) to the UM100 and UM55 by $z/\langle z_i \rangle \approx 1.0$. The wind is predominantly from the south in all models as expected based on measurements made at URAO (see Sect. 2.1). The UKV x-component of the wind (u) decreases more strongly with height and is ~ 2 m s^{-1} larger than u in the UM100 and UM55. Also, unlike the UM100 and UM55, the UKV u has a distinct minimum in the capping inversion before increasing rapidly above.

The UKV sub-grid (i.e., parameterised) (Fig. 2d) and total (Fig. 2f) turbulent passive scalar fluxes decrease linearly with height from the ground to $z/\langle z_i \rangle \approx 1.1$ where $c = 0$, as expected for a quasi-steady-state CBL (Wyngaard and
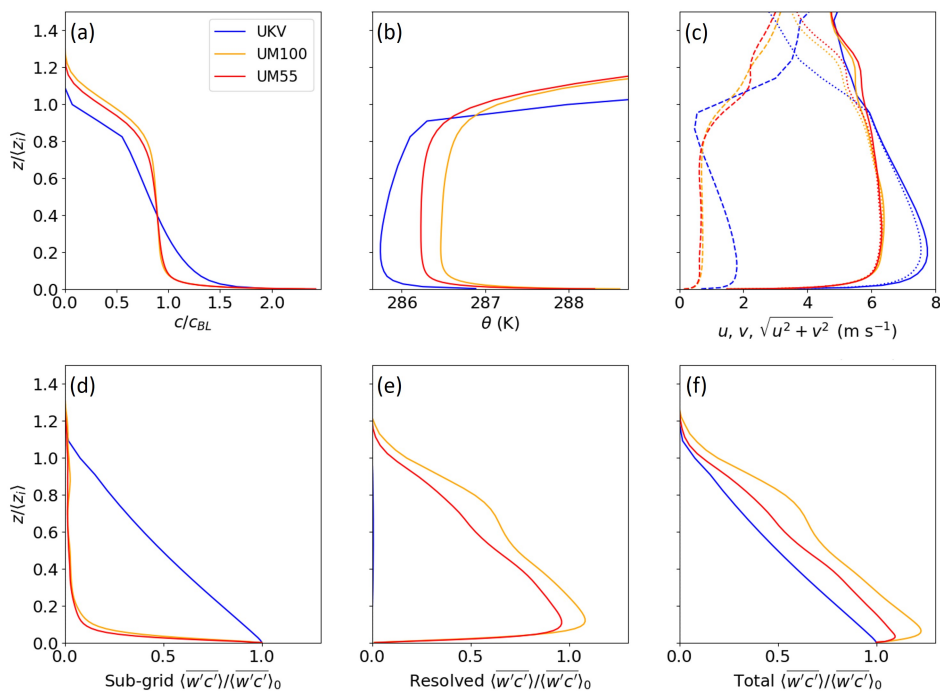
FIGURE 2   Horizontally-averaged profiles in analysis region 1 at 13:00 UTC – (a) continuous release passive scalar concentration normalised by the average concentration in the BL, (b) potential temperature, (c) x-component of wind u (dashed line), y-component of wind v (dotted line), and wind speed (solid line), (d) sub-grid passive scalar flux, (e) resolved passive scalar flux, and (f) total passive scalar flux. The y-axis is height above the ground normalised by the horizontally-averaged boundary layer height which is 1608, 1475, and 1439 m for the UKV, UM100, and UM55, respectively.

Brost, 1984). The sub-grid and total fluxes are to a very good approximation equal because at O(1 km) grid lengths turbulent transport is not resolved within the CBL, as seen for the UKV in Fig. 2e.

The UM100 and UM55 sub-grid fluxes (Fig. 2d) decrease rapidly in the surface layer (and slightly faster for the UM55), before decreasing more gradually to zero where $c = 0$ at $z/\langle z_i \rangle \approx 1.2$. Above the surface layer, the UM100 and UM55 resolved fluxes (Fig. 2e) dominate the total fluxes (Fig. 2f). The total fluxes decrease approximately linearly between $z/\langle z_i \rangle \approx 0.1 - 1.2$. Unlike the UKV, the UM100 (in particular) and UM55 have a small increase in total flux in the surface layer. This is likely due to non-conservation issues with grid-scale turbulence close to the surface (as discussed in Sect. 2.3). The sub-grid / resolved flux partitioning for passive scalar here is consistent with that of Lean et al. (2019) for heat fluxes.

By considering the flux profiles and theory it is possible to interpret the differences between the UKV and UM100/UM55 c and θ profile behaviour in the mixed layer. In the MetUM, the total vertical turbulent flux for a scalar variable χ is given by (Lock et al., 2016)

$$\overline{w'\chi'}_{tot} = \overline{w'\chi'}_{res} + \overline{w'\chi'}_{sbg}, \tag{1}$$
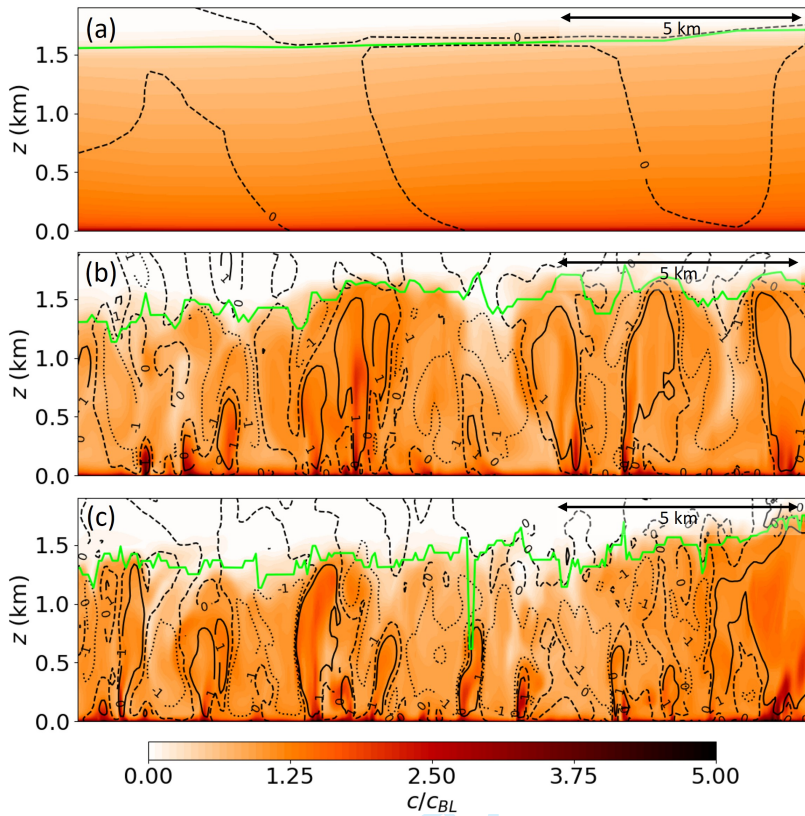
FIGURE 3 (a) UKV, (b) UM100, and (c) UM55 vertical cross-sections at 13:00 UTC approximately perpendicular to the mean-flow in the BL (see location in Fig. 1b) showing continuous release passive scalar concentration normalised by the average concentration in the BL. Black solid, dashed, and dotted lines are -1, 0 and 1 m s^{-1} vertical velocity contours, respectively. The lime solid line is BL scheme diagnosed z_i.

where $\overline{w'\chi'}_{res}$ is the resolved flux and $\overline{w'\chi'}_{sbg}$ is the sub-grid flux given by

$$\overline{w'\chi'}_{sbg} = -\max\left[W_{1D}K_\chi^{NL}, K_\chi(Ri)\right]\frac{\partial \chi}{\partial z} + W_{1D}K_\chi^{NL}\gamma_\chi. \qquad (2)$$

The weighting function W_{1D} controls the amount of sub-grid flux mixing and is given by

$$W_{1D} = 1 - \tanh\left(0.15\frac{z_i}{\Delta}\right)\max\left[0, \min\left[1, \frac{4}{15}\left(4 - \frac{\Delta}{z_i}\right)\right]\right]. \qquad (3)$$

It is a function of the dimensionless parameter Δ/z_i, and is designed to give the proportion of TKE that is resolved versus sub-grid in LES at various horizontal grid lengths (Honnert et al., 2011; Boutle et al., 2014). Between 11:00 UTC and 14:00 UTC the average weighting function values are 0.15, 0.95, and 1.00 for the UKV, UM100, and UM55, respectively. This means that the mixed-layer turbulence is treated by the UKV as 85% parametrised, and 95% and 100% resolved in the UM100 and UM55, respectively (i.e., to a good approximation the UM100 and UM55 are in LES mode). K_χ^{NL} is a non-local diffusivity, $K_\chi(Ri)$ is a local diffusivity, Ri is the local Richardson number, and γ_χ is a height

independent parameter determined by the surface and entrainment fluxes. In the surface layer, the local sub-grid flux term begins to dominate the non-local sub-grid flux terms (Eq. 2), and towards the surface the turbulence becomes increasingly parametrised rather than resolved. The γ_χ term is a counter-gradient flux term that is independent of local gradients, and is included to make χ profiles more well-mixed. However, it is only included when $\chi = \theta$. Specific humidity profiles tend to decrease in the upper CBL due to drying at the mixed-layer top, so for them the extra non-local term is not included (Lock et al., 2016). Passive scalars do not have their own tailored treatment in the MetUM, so have no counter-gradient term (Lock et al., 2016).

Given that the UKV θ profile (Fig. 2b) increases more than expected in the mixed layer based on the CBL literature (Garratt, 1994; Pleim, 2007), and that the UM100 and UM55 are more constant with height, it is likely that the counter-gradient term is not large enough to maintain a constant θ profile. Also, the absence of the counter-gradient term for c is likely why it decreases by approximately half in the mixed layer for the UKV, but decreases by only $\approx 10\%$ for the UM100 and UM55 where mixed layer turbulence is almost all resolved.

Figures 3a-c show vertical cross-sections approximately perpendicular to the mean flow of continuous-release passive scalar concentration for the UKV, UM100, and UM55, respectively. The UKV field is smooth as expected because the CBL turbulence is not resolved at O(1 km) grid length. In the UM100 and UM55, passive scalar converges near the surface into updrafts that are associated with high concentrations. The updrafts branch in the upper BL, due to the capping inversion forcing air to spread horizontally, before descending in downdrafts that are broader and have lower concentrations. Sometimes updrafts do not span the entire BL, which is expected because downdrafts act to suppress the less energetic updrafts beneath, and instantaneous fields can contain updrafts that have not had time to fully develop. The resolved motions in the UM100 and UM55 are typical of those observed in idealised LES and experiments (Deardorff, 1972b; Willis and Deardorff, 1979). This is perhaps not surprising considering that the UM100 and UM55 are approximately in LES mode, but nonetheless it is important to demonstrate that CBL turbulence is well represented in hectometric NWP for realistic meteorology.

There is clearly more spatial detail in the UM55 than UM100 concentration and vertical velocity fields. However, it is not immediately obvious whether the integral scale turbulence (i.e., O(z_i) updrafts, downdrafts, and their spacing) is the same in the UM100 and UM55. The convergence of the UM100 and UM55 is examined in greater detail in Sect. 3.1.2.

3.1.2 | Horizontal Structure

The non-dimensional ratio $-z_i/L_O$ with L_O the Obukhov length (Garratt, 1994) can be used to characterise the turbulent structure in CBLs (Salesky et al., 2017). We use values from our simulations to interpret whether the turbulence structure is as expected compared to the literature. Figure 4 shows horizontal cross-sections of continuous-release c and w for the UM100 and UM55 at $z/\langle z_i \rangle = 0.1$, $z/\langle z_i \rangle = 0.5$, and $z/\langle z_i \rangle = 1.0$ at 13:00 UTC. The ratio is approximately 28 and 30 for the UM100 and UM55, respectively. The UKV is not shown since the fields are smooth (Fig. 3). The UM100 and UM55 vertical velocity fields at $z/\langle z_i \rangle = 0.1$ (Fig. 4a,b) are qualitatively similar with Fig. 4 of Salesky et al. (2017), where the same field is shown, but generated using LES of a CBL with $-\langle z_i \rangle/L_O = 26$. The turbulence although elongated in the streamwise direction, retains some open cell like structure typical of buoyancy-dominated CBLs ($-\langle z_i \rangle/L_O \gg 20$). Salesky et al. (2017) showed that the largest changes in CBL structure occur around $-\langle z_i \rangle/L_O = 15 - 20$, and for more shear dominated conditions ($-\langle z_i \rangle/L_O < 15$) horizontal convective rolls develop with little or no turbulent structure in the cross-stream.

The structure of the CBL can be further understood by inspecting the vertical velocity at $z/\langle z_i \rangle = 0.5$ (Fig. 4e,f) and $z/\langle z_i \rangle = 0.1$ (Fig. 4a,b). With increasing height the UM100 and UM55 updrafts become broader, updrafts and
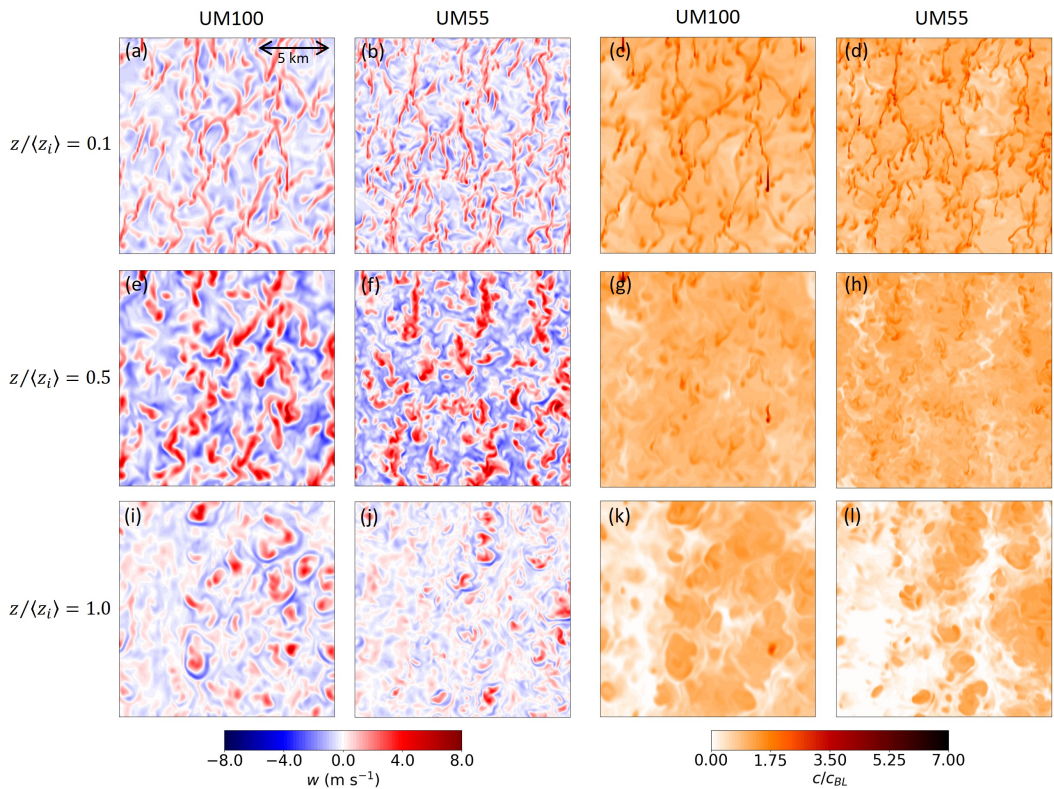
FIGURE 4 Horizontal cross-sections of vertical velocity (columns 1 and 2 – a,b,e,f,i,j) and continuous-release passive scalar concentration normalised by the average concentration in the BL (columns 3 and 4 – c,d,g,h,k,l), for $z/\langle z_i \rangle = 0.1$ (row 1 – a,b,c,d), $z/\langle z_i \rangle = 0.5$ (row 2 – e,f,g,h), and $z/\langle z_i \rangle = 1.0$ (row 3 – i,j,k,l). The UM55 columns are 1 (a,e,i) and 3 (c,g,k), and the UM100 columns are 2 (b,f,j) and 4 (d,h,l). See Fig. 1b for location.

downdrafts are stronger, and less smaller scale turbulence is apparent. This is consistent with some updrafts not spanning the entirety of the CBL (Sect. 3.1.1) and merging of smaller updrafts to form broader ones (Schmidt and Schumann, 1989). At $z/\langle z_i \rangle = 1.0$ (Fig. 4i,j) the updrafts reach the capping inversion where they spread horizontally into domes, becoming less aligned with the flow.

It is clear from the c horizontal cross-sections in Fig. 4 that c correlates strongly with w. The standard deviation of c normalised by the average concentration in the layer ($\langle c \rangle$) is calculated at $z/\langle z_i \rangle = 0.1$ at 13:00 UTC in analysis region 1 (Fig. 1b). For both the UM100 and UM55 the value is 0.32. Assuming a Gaussian distribution one would expect 2.1% of values to be greater than the mean plus two times the standard deviation ($= 1.64\langle c \rangle$). However, the distribution exhibits positive skewness, with approximately 5% of values greater than $1.64\langle c \rangle$, making large values of c more likely compared to a Gaussian distribution. It is perhaps surprising that $30 - 45$ km downstream of the southern edge of the homogeneous continuous release source that c is often considerably larger than its mean value. Passive scalar emitted near the southern edge of the source region has time to become well-mixed $30 - 45$ km downstream, yet it does not totally dominate the near-surface passive scalar concentration. This is because local emissions that converge into updrafts can still lead to considerable horizontal heterogeneity. This raises the question of whether

convergence at the base of updrafts causes significant transient surface level pollution concentration heterogeneity in cities. Investigation would need to account for building-scale turbulence so experimental methods or building-resolving LES would be suitable.

We note that in the UM100 horizontal cross-sections there is some evidence of grey zone issues. Grid scale updrafts align with the grid at $z/\langle z_i \rangle = 0.1$ (Figs. 4a,c), causing large c and w throughout the CBL (Figs. 4e,g,i,k) (Blunn, 2021, Fig. 3.15).

There is more detailed turbulent structure in the UM55 than UM100 (Fig. 4), but as in Sect. 3.1.1 it is not clear whether the integral scale $O(z_i)$ CBL eddies are fully resolved by the UM100. While we do not assume the UM55 fully resolves the integral scale turbulence, it can be used as a reference for the UM100, to test convergence with decreasing Δ. Convergence is investigated using the two-point cross-correlation function, which for two variables χ_1 and χ_2 at height z is given by

$$R_{\chi_1 \chi_2}(L) = \frac{\langle (\chi_1(l) - \langle \chi_1 \rangle)(\chi_2(l') - \langle \chi_2 \rangle) \rangle}{\langle (\chi_1(l) - \langle \chi_1 \rangle)(\chi_2(l) - \langle \chi_2 \rangle) \rangle}, \tag{4}$$

where $L \equiv l - l'$ is the spatial separation between l and another point l', and $\langle \rangle$ is the horizontal spatial average. When calculating R_{ww} for $l = x$ (i.e., R_{ww}^x cross-correlations along the east-west axis), the cross-correlation is calculated at each y, then averaged, and vice-versa for $l = y$ (i.e., R_{ww}^y cross-correlations along the north-south axis). The term turbulence integral length scale will be used to mean any length scale that characterises the largest turbulence scale. This includes updraft width and separation, and statistical measures.

Plotted in Fig. 5 is R_{ww} for the UM100 and UM55 in analysis region 1 at 13:00 UTC, for $z/\langle z_i \rangle = 0.1$ and $z/\langle z_i \rangle = 0.5$, with $l = x$ and $l = y$. The first R_{ww}^x zero-crossing corresponds to the typical updraft width. Values are calculated at 11:00, 12:00, 13:00, and 14:00 UTC, and the averages and standard deviations (σ) (calculated over the four times) for the UM100 and UM55 are given in Table 2. The four times are chosen because the CBL was fairly consistent then (with $-\langle z_i \rangle / L_{MO} = 29.3 \pm 2.6$ and $-\langle z_i \rangle / L_{MO} = 29.8 \pm 2.1$ for the UM100 and UM55, respectively), and to enable the differences in R_{ww} characteristics between the two models to be compared with consideration of the statistical uncertainty associated with using instantaneous snapshots. At $z/\langle z_i \rangle = 0.1$, the first R_{ww}^x zero-crossing is $(0.235 \pm 0.006)\langle z_i \rangle$ and $(0.208 \pm 0.005)\langle z_i \rangle$, for the UM100 and UM55, respectively. The zero crossings at $z/\langle z_i \rangle = 0.5$ are $(0.419 \pm 0.026)\langle z_i \rangle$ and $(0.446 \pm 0.044)\langle z_i \rangle$, for the UM100 and UM55, respectively. Updrafts in both models are approximately twice as wide at $z/\langle z_i \rangle = 0.5$ compared to $z/\langle z_i \rangle = 0.1$.

TABLE 2 The average and standard deviation of the turbulence integral length scale values for the UM100 and UM55 calculated at $z/\langle z_i \rangle = 0.1$ and $z/\langle z_i \rangle = 0.5$ from R_{ww}^x and R_{ww}^y. The average and standard deviation are calculated from values at 11:00, 12:00, 13:00, and 14:00 UTC. The unit of all length scales is $\langle z_i \rangle$.

Turbulence integral length scale	$z/\langle z_i \rangle = 0.1$		$z/\langle z_i \rangle = 0.5$	
	UM100	UM55	UM100	UM55
First R_{ww}^x zero-crossing	0.235±0.006	0.208±0.005	0.419±0.026	0.446±0.044
Second R_{ww}^x zero-crossing	1.446±0.274	1.544±0.300	1.711±0.281	1.767±0.254
$\int_0^{L_{0.1}} R_{ww}^y \, dL$	0.257±0.016	0.213±0.009	0.371±0.025	0.359±0.070

For L greater than the first R_{ww}^x zero-crossing and smaller than the second R_{ww}^x zero-crossing, there is a minima where the updrafts are anti-correlated with the downdrafts. The second R_{ww}^x zero-crossing corresponds to where
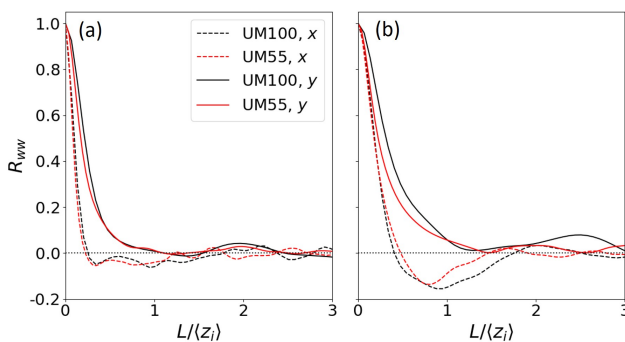
FIGURE 5   Vertical velocity two-point cross-correlation functions plotted against $L/\langle z_i \rangle$ at 13:00 UTC for (a) $z/\langle z_i \rangle = 0.1$ and (b) $z/\langle z_i \rangle = 0.5$. Black and red lines correspond to the UM100 and UM55, respectively, and dashed and solid lines correspond to cross-correlations along the x- and y-axes, respectively.

the updrafts come back in phase, and therefore represents the cross-stream updraft separation. Its values are given in Table 2. In both models the cross-stream updraft separation increases only slightly from $\approx 1.5\langle z_i \rangle$ to $\approx 1.74\langle z_i \rangle$ between $z/\langle z_i \rangle = 0.1$ and $z/\langle z_i \rangle = 0.5$. The updraft width increases more strongly with height than the cross-stream updraft separation. The updraft width to cross-stream updraft separation ratio is approximately 0.15 and 0.25 at $z/\langle z_i \rangle = 0.1$ and $z/\langle z_i \rangle = 0.5$, respectively, for both the UM100 and UM55.

The updrafts are generally aligned in the streamwise direction, have finite streamwise length, and meander in the cross-stream direction. As the w fields are increasingly separated, the updrafts eventually become uncorrelated, with the streamwise cross-correlations, R_{ww}^{y}, having no prominent negative minima, since there is little streamwise repetitive turbulence structure. Therefore, zero-crossings cannot be used to define the turbulence integral length scale. A common alternative method for calculating the turbulence integral scale is to integrate the two-point cross-correlation function $\int_0^\infty R_{ww} dL$ (Dosio et al., 2005). Here we take the upper integral limit to be the separation at which $R_{ww}^{y} < 0.1$ ($L_{0.1}$), so that any large scale structures ($L \gg O(z_i)$) in the w field unrelated to turbulence are not included.

The streamwise turbulence integral length scale $\int_0^{L_{0.1}} R_{ww}^{y} dL$ at $z/\langle z_i \rangle = 0.1$ is $(0.257 \pm 0.016)\langle z_i \rangle$ and $(0.213 \pm 0.009)\langle z_i \rangle$ for the UM100 and UM55, respectively, where the averages and standard deviations are over times 11:00, 12:00, 13:00, and 14:00 UTC. The values are $> 2\sigma$ from each other suggesting that the UM55 streamwise turbulence integral length scale is generally smaller than for the UM100. The streamwise turbulence integral length scale at $z/\langle z_i \rangle = 0.5$ is $(0.371 \pm 0.025)\langle z_i \rangle$ and $(0.359 \pm 0.070)\langle z_i \rangle$ for the UM100 and UM55, respectively. Again the UM55 streamwise turbulence integral length scale is slightly smaller than that for the UM100, but they are within σ of one another so this could be due to statistical variation in time.

The first R_{ww}^{x} zero-crossing is $> 3\sigma$ smaller for the UM55 than the UM100 at $z/\langle z_i \rangle = 0.1$. However, the UM100 and UM55 values are within σ of each other for the first R_{ww}^{x} zero-crossing at $z/\langle z_i \rangle = 0.5$, and the second R_{ww}^{x} zero-crossings at $z/\langle z_i \rangle = 0.1$ and $z/\langle z_i \rangle = 0.5$.

So for the R_{ww}^{x} first zero-crossing at $z/\langle z_i \rangle = 0.1$ and R_{ww}^{y} integral length scale at $z/\langle z_i \rangle = 0.1$ where mean values are $> 3\sigma$ and $> 2\sigma$ away from each other, respectively, the UM55 turbulence scales are smaller than the UM100. This suggests that near the top of the surface layer (often considered to be $z/\langle z_i \rangle \approx 0.1$) the UM100 integral scale turbulence has not converged. However, in the middle of the CBL, where smaller scale turbulence associated with the surface layer has merged into larger updrafts spanning the CBL, the UM100 is demonstrating signs of convergence.

Lean et al. (2022) conducted 100 m, 55 m, and 25 m Δ UM simulations for a clear-sky day with $z_i \approx 750$ m. At

$z/z_i = 0.4$ they found no signs of updraft width convergence. This is consistent with the behaviour at $z/\langle z_i \rangle = 0.1$ rather than $z/\langle z_i \rangle = 0.5$ in our study. This could in part be due to updrafts at $z/z_i = 0.4$ being nearer the surface and therefore narrower than at $z/z_i = 0.5$, but more likely it is because z_i is approximately a factor of two smaller in the Lean et al. (2022) simulations, so that the turbulence is smaller scale and updrafts are narrower. From power spectra at $z/z_i = 0.25$, at energy producing scales Lean et al. (2019) found modelled turbulence to be most similar to observed turbulence for $\Delta = 25$ m. This suggests that to fully represent the integral scale turbulence in the lower portion of the CBL at least $\Delta = 25$ m is required. However, for deep CBLs (O($z_i = 1.4$ km)), particularly towards the middle of the CBL, our study suggests that some integral scale properties of the turbulence (e.g., cross-stream updraft separation) start to show signs of convergence at $\Delta = 100$ m.

3.2 | Vertical Evolution Following Puff Release

In this section, the evolution of the vertical profile of the passive scalar field is investigated for the UKV, UM100, and UM55. A qualitative investigation is made using vertical cross-sections and vertical profiles of the puff release passive scalar concentrations. Timescales associated with the vertical mixing in each model are investigated in Sect. 3.3.

Figure 6 shows vertical cross-sections of the UKV (a-c) and UM55 (d-f) 13:00 UTC puff-release passive scalar at 5, 20, and 55 min since release. The cross sections are approximately perpendicular to the flow (see location in Fig. 1b). At 13:05 UTC the UKV passive scalar concentration is very horizontally homogeneous and high near to the surface, but the UM55 concentration is much more horizontally and vertically heterogeneous, with high concentration values at greater heights than the UKV. These high values can be found up to $z = 1$ km and are associated with updrafts resolved in the UM55. At 13:20 UTC the UKV concentration is still higher near the surface and lower near the top of the BL, but the vertical gradient is reduced. At the same time there is more passive scalar in the upper BL than lower BL for the UM55. Therefore, the lift-off behaviour seen in experiments and LES is demonstrated here (Deardorff, 1972b; Willis and Deardorff, 1976). By 13:55 UTC the UKV concentration field is very homogeneous throughout the BL. The UM55 concentration field has become much more homogeneous, but vertical and horizontal structure still remains.

Differences in the vertical evolution of passive scalar concentration between models can be further understood by inspecting vertical profiles. Figure 7 shows the 13:00 UTC puff-release concentration profiles for the UKV, UM100, and UM55 in analysis region 1 (Fig. 1b) at 5 min intervals. The UKV concentration profiles decrease and increase monotonically with time near the surface and in the upper BL, respectively, and tend towards a steady state. The UKV concentration decreases monotonically with height at all times. The UM100 and UM55 profiles are most similar to the UKV profile at 5 min, which is likely due to vertical mixing near the surface being partly parameterised in all models. However, after 10 min the UM100 and UM55 have a much larger proportion of passive scalar in the upper BL than the UKV. Between approximately 15–30 min the UM100 and UM55 have more passive scalar in the upper BL than the lower BL. The surface level concentrations 20 min after release are approximately three times lower for the UM55 than the UKV. The lofting of passive scalar emitted at the surface is thus an important process controlling surface level pollution concentration.

By 13:40 UTC the UM100 and UM55 profiles change very little with time, and decrease by less than 20% between the surface and $z/\langle z_i \rangle = 0.8$ (i.e., are "well-mixed"), despite the passive scalar heterogeneity seen in Fig. 6f. The UM100 and UM55 profiles are very similar across times, demonstrating that the lower resolution UM100 represents the most important passive scalar CBL turbulent mixing processes.
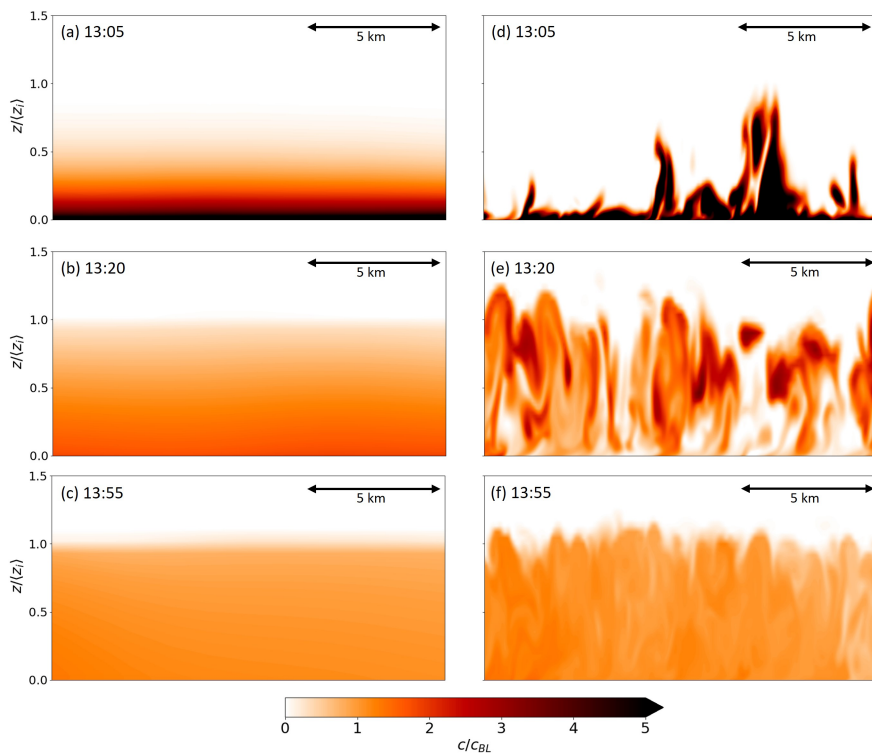
FIGURE 6 Vertical cross-sections approximately parallel to the mean-flow in the BL (location Fig. 1b) showing puff-release passive scalar concentration normalised by the average concentration in the BL. (a,b,c) are the UKV at 13:05, 13:20, and 13:55 UTC, respectively, and (d,e,f) are the UM55 at 13:05, 13:20, and 13:55 UTC, respectively.

3.3 | Dispersion Timescales

It was seen in previous sections that the UKV and UM100/UM55 have different vertical mixing behaviour, and that passive scalar is more efficiently mixed in the UM100/UM55 (e.g. Fig. 2a). Here, a reduced analytical model is developed that enables the vertical mixing characteristics exhibited by the models to be attributed to different dispersion processes (i.e., diffusive and ballistic). Vertical mixing timescales associated with the processes are derived by fitting the reduced analytical model to the NWP output. The differences in vertical mixing behaviour between models are thus quantified.

The height of passive scalar may be characterised by the centre of mass

$$\text{CoM} = \frac{\int_A \int_0^\infty c(x, y, z) z \, dz \, dA}{\int_A \int_0^\infty c(x, y, z) \, dz \, dA}, \tag{5}$$

where A is the area of the analysis region (taken here to be analysis region 1). By tracking the CoM trajectory with time one can obtain an estimate of how well-mixed the passive scalar is, since, assuming that the amount of passive scalar that escapes the BL is negligible, $\text{CoM}/\langle z_i \rangle \to 0.5$ in the limit of being well-mixed.

The Lagrangian stochastic modelling approach is based on calculating an ensemble of particle trajectories through
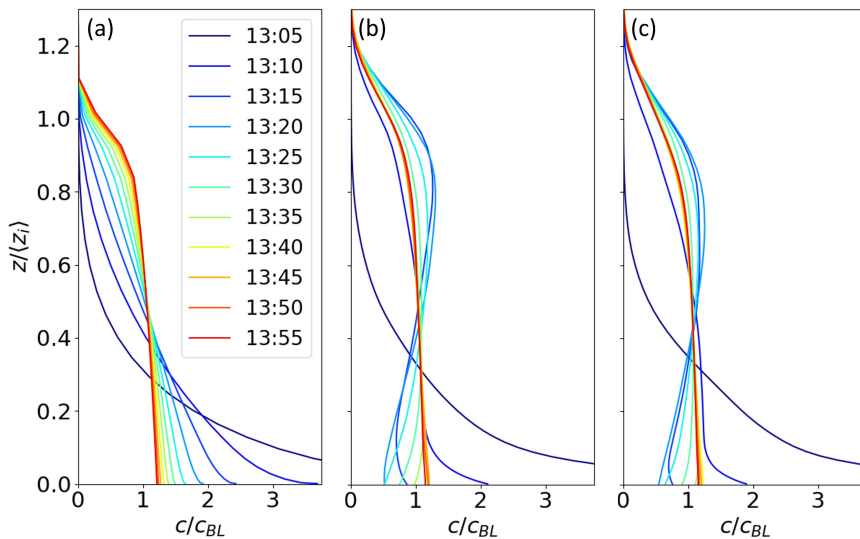
FIGURE 7   Time evolution of the 13:00 UTC puff-release concentration profiles for the (a) UKV, (b) UM100 and (c) UM55 models. Profiles are calculated in analysis region 1 (see location in Fig. 1b).

a turbulent flow, given knowledge of Eulerian velocity statistics. The ensemble average of such trajectories defines the concentration distribution. The mathematical form of most Lagrangian stochastic models (LSMs) is that of the generalised Langevin equation (Thomson and Wilson, 2012). Importantly it has the correct dispersion behaviour in the ballistic ($t \ll \tau$) and diffusive ($t \gg \tau$) limits.

As argued in Appendix 1, if various simplifying assumptions about CBL turbulence hold, then the evolution of the CoM can be roughly approximated by:

$$\ddot{\tilde{Z}} = -2\gamma\dot{\tilde{Z}} - \omega^2\tilde{Z}. \tag{6}$$

where $\tilde{Z} \equiv \tilde{z} - \langle z_i \rangle/2$, $\tilde{z}$ is the ensemble average (tilde) height of a LSM's passive scalar particles and is equivalent to the CoM, $\omega = 2\pi/\tau_\omega$ is the natural frequency (which is related to the eddy turnover timescale), and $\gamma = 1/(2\tau)$ determines the amount of damping. This is the form of a damped simple harmonic oscillator (DSHO). The first, "damping", term on the right-hand side represents the diffusive dispersion caused by smaller eddies, which cause particles to lose memory of the CBL-spanning eddy into which each particle was initially released. The second term on the right hand side is an approximation to the LSM drift term (see Appendix 1), which offsets the tendency of particles to accumulate in areas of low vertical velocity variance, and is related to turbulent motions induced by pressure gradients in the CBL i.e., O(z_i) overturning eddies (Thomson, 1987).

The general solution to Eq. 6 is given by

$$\tilde{Z}/\langle z_i \rangle = Ae^{p_+t} + Be^{p_-t} = e^{-\gamma t}\left(Ae^{\sqrt{\gamma^2 - \omega^2}t} + Be^{-\sqrt{\gamma^2 - \omega^2}t}\right), \tag{7}$$

where A and B are dimensionless constants, and $p_\pm = -\gamma \pm \sqrt{\gamma^2 - \omega^2}$. We can consider two regimes – overdamped ($\gamma > \omega$) and underdamped ($\gamma < \omega$) where dispersion is diffusive and ballistic dominated, respectively. In the diffusive

limit ($\gamma \gg \omega$) $p_+ \to 0$ and $p_- \to -2\gamma$, so that there is effectively one decay term in Eq. 7. We define two timescales $\tau_{p_\pm} = -1/p_\pm$ such that in the diffusive limit $\tau_{p_+} \to \infty$ and $\tau_{p_-} \to 1/(2\gamma) = \tau$. τ is a memory timescale characterising how long it takes the motion of a particle to become uncorrelated with the motion of the particle immediately after release (see Appendix 1).

For a ground release $\tilde{z}(0)/\langle z_i \rangle = 0$, it follows from Eq. 7 that $A + B + 0.5 = 0$. The overdamped case of Eq. 7 can then be written as

$$\tilde{z}/\langle z_i \rangle = 0.5 + A e^{p_+ t} - (0.5 + A) e^{p_- t}, \tag{8}$$

where $p_+, p_- < 0$, and the underdamped case can be written as

$$\tilde{z}/\langle z_i \rangle = 0.5 \left[1 - \frac{e^{-\gamma t} \cos(\Omega t + \phi)}{\cos(\phi)} \right], \tag{9}$$

where ϕ is a phase constant and $\Omega = \sqrt{\omega^2 - \gamma^2}$. Both solutions have two effective time parameters: $\tau_{p_-} = -1/p_-$ and $\tau_{p_+} = -1/p_+$ (overdamped), and $\tau = 1/(2\gamma)$ and $\tau_\Omega = 2\pi/\Omega$ (underdamped). A critically damped solution occurs when $\gamma = \omega$, and is given by

$$\tilde{z}/\langle z_i \rangle = 0.5 + (-0.5 + Jt) e^{-\gamma t}, \tag{10}$$

where J is a constant.

The overerdamped solution (Eq. 8) exponentially decays with two timescales towards $\tilde{z}/\langle z_i \rangle = 0.5$ without oscillating. When ω is only slightly smaller than γ, then the two timescales $\tau_{p_\pm}$ in the exponential terms are both approximately equal to 2τ. As ω becomes increasingly smaller than γ, τ_{p_+} becomes larger than τ_{p_-}, until as discussed previously in the diffusive limit $\tau_{p_+} \to \infty$ and $\tau_{p_-} \to \tau$. The underdamped solution (Eq. 9) oscillates at frequency Ω (slower than ω) with amplitude exponentially decaying to zero with e-folding lifetime $1/\gamma = 2\tau$, so that $\tilde{z}/\langle z_i \rangle$ tends towards 0.5. For a near-ground release, increasing ω results in $\tilde{z}$ moving more quickly from the surface since the oscillations are faster. Also, as ω becomes larger relative to γ (i.e., increasingly ballistic dominated dispersion), the oscillations are more prominent and $\tilde{z}/\langle z_i \rangle$ overshoots 0.5 more, since the solution has undergone less decay by the time of maximum amplitude.

The optimal fits between Eqs. 8 and 9 and the UKV, UM100, and UM55 puff release $\tilde{z}$ timeseries are found by varying the parameter values and minimising the root mean square error. Figure 8 shows these timeseries and the fitted analytical solutions for a puff release at 13:00 UTC. The solutions reproduce the salient features of the simulation results. The UKV is best fit by the overdamped solution, and $\tilde{z}/\langle z_i \rangle$ tends increasingly slowly with time towards 0.5. The UM100 and UM55 are best fit by the underdamped solution, where $\tilde{z}/\langle z_i \rangle$ increases rapidly, and overshoots $z/\langle z_i \rangle = 0.5$ after ≈ 15 min, before settling at ≈ 0.5. Also, the eddy turnover timescale $\tau_w = 105.2$ min is much slower than the decorrelation timescale $\tau = 6.7$ min, consistent with the lack of ballistic type dispersion in the UKV.

The best fit parameter values for puff releases at 11:00, 12:00, 13:00, and 14:00 UTC are calculated, and their average values are given in Table 3. These times are selected as they are highly convective and the CBL is quasi-stationary with $1.4 < z_i < 1.6$ km across all models. For the UKV, τ_{p_-} and τ_{p_+} are 8.4 and 33.6 min, respectively. The τ_{p_-} term in Eq. 8 decays quickly and largely determines the short timescale dispersion behaviour. The τ_{p_+} term decays more slowly and largely determines the time it takes for passive scalar to become well-mixed.

For the UM55, τ and τ_w are 4.6 and 33.3 min, respectively, and for the UM100 τ and τ_w are 5.7 and 36.0 min, re-
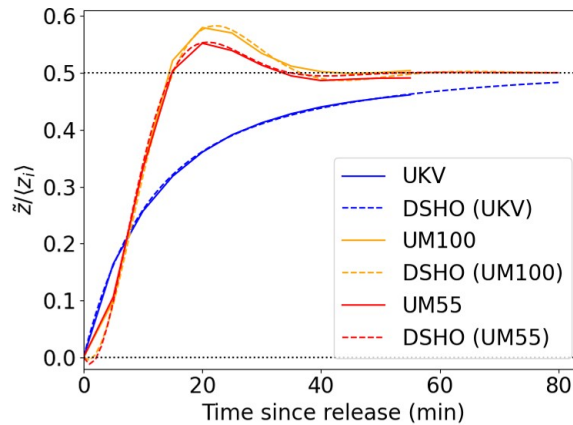
FIGURE 8 UKV, UM100 and UM55 model CoM trajectories for a puff release at 13:00 UTC (solid) with optimal DSHO solutions (dashed). The trajectories and optimal solutions are also qualitatively representative of releases at 11:00, 12:00, and 14:00 UTC.

TABLE 3 Average optimal fit DSHO parameter values to the UKV, UM100, and UM55 CoM trajectories. The average is over the values at 11:00, 12:00, 13:00, and 14:00 UTC. $\tau_{p_+} = -1/p_+, \tau_{p_-} = -1/p_-, \tau_\Omega = 2\pi/\Omega, \tau = 1/(2\gamma)$, and $\tau_\omega = 2\pi/\omega$. Note $B = -A - 0.5$. Also included is the convective timescale $t_* = \langle z_i \rangle / w_*$. The unit of all timescales is minutes.

Model	A	ϕ	τ_{p_+}	τ_{p_-}	τ	τ_Ω	τ_ω	t_*
UKV	-0.21	-	33.6	8.4	6.7	-	105.2	11.9
UM100	-	-38°	-	-	5.7	41.8	36.0	11.9
UM55	-	-44°	-	-	4.6	40.8	33.3	11.6

spectively. This means that the resolved overturning motions associated with ballistic dispersion have a short enough timescale ($\tau_\omega < 4\pi\tau$ i.e., underdamped $\gamma < \omega$) to cause the CoM to overshoot $\langle z_i \rangle/2$ (see Fig. 8), so that more passive scalar is in the upper than the lower half of the CBL. The τ decay term in Eq. 9 controls how quickly $\tilde{z}/\langle z_i \rangle$ reaches a steady state value of 0.5 (i.e., becomes well-mixed). Thus the timescale that determines how quickly the models become well-mixed is $\tau_{p_+}/(2\tau) \approx 3$ times longer for the UKV than the UM100/UM55, consistent with the UKV vertical mixing being less efficient in Sect. 3.1.1. The UM55 having slightly smaller τ and τ_Ω than the UM100 is consistent across times (not shown), suggesting that the UM100 and UM55 vertical mixing has small differences, and has not converged at $\Delta = 100$ m.

The convective time scale $t_* = \langle z_i \rangle / w_*$, where w_* is the convective velocity-scale (Garratt, 1994), is 11.9 and 11.6 min for the UM100 and UM55, respectively. Its value is $t_* \approx 2\tau$ in the UKV overdamped solution, while $t_* \sim \tau_\omega/3$ for the underdamped cases.

At very short times (0-5 min) the vertical mixing is slightly more efficient in the UKV than the UM100/UM55 (Fig. 8). This is possibly due to the vertical grid length being ~ 2 times larger in the UKV compared to the UM100/UM55, influencing parameterised vertical mixing near the surface. The best fit UM100/UM55 solutions have $\phi = -44°$ on average. This results in $\tilde{z}/\langle z_i \rangle$ becoming negative for a very short time, before becoming positive and increasing

rapidly. This unphysical behaviour is a limitation of the model. That the optimal fit has $\phi \neq 0$ is likely a consequence of assuming that turbulence is vertically homogeneous in the first and third terms on the right hand side of Eq. 13.

3.4 | City-Scale Near-surface Concentration Dependence On Vertical Mixing

It was demonstrated in Sections 3.2 and 3.3 that unlike passive scalar in the UKV, passive scalar in the UM100 and UM55 is higher concentration in the upper half of the CBL at times $\approx \tau_\Omega/2$ since puff release (i.e., half the time period of the underdamped DSHO). This is due to the UM100 and UM55 representing the lift-off behaviour that occurs in the ballistic dispersion limit. In this section, we investigate the influence of representing (UM100 and UM55) versus not representing (UKV) the lift-off effect on passive scalar vertical distribution evolution with downstream distance over London. A homogeneous continuous ground-source of passive scalar represents idealised city-scale pollution emissions. Figure 9a shows the UKV and UM55 profiles normalised by the mean concentration within the BL at 13:00 UTC. The profiles are calculated in five west-east bands across analysis region 2 (see location in Fig. 1b) at 0-10 km, 10-20 km, 20-30 km, 30-40 km and 40-50 km downstream distance of the southern edge of the source.
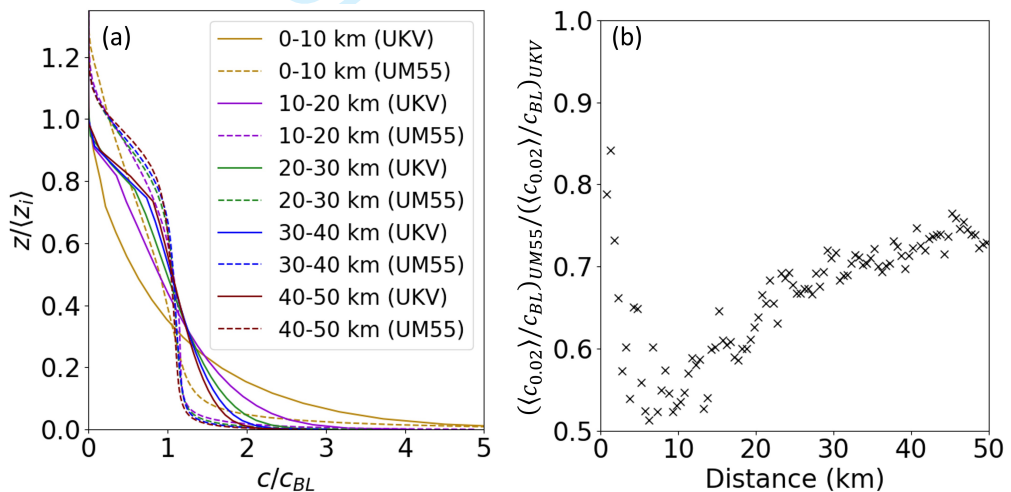
FIGURE 9 (a) UKV and UM55 continuous-release passive scalar concentration profiles normalised by the average concentration in the BL at 13:00 UTC. Concentrations are calculated in five west-east bands across analysis region 2 (see location in Fig. 1b) – 0-10 km, 10-20 km, 20-30 km, 30-40 km and 40-50 km downstream of the southern edge of the source. (b) Ratio of the UM55 to UKV continuous-release passive scalar concentration at $z/\langle z_i \rangle = 0.02$ normalised by the average concentration in the BL at 13:00 UTC. The ratio is calculated in analysis region 2 at 0.5 km intervals downstream of the southern edge of the source.

The downstream distance (D) at which the profiles become steady state can be used to understand the efficiency of vertical mixing. Profiles become steady state when the majority of passive scalar is well mixed, which occurs at smaller D with increasing vertical mixing efficiency. For all models, immediately downstream of the source edge the passive scalar is near the surface, and with increasing D more of the passive scalar has time to become well mixed. The UKV profiles tend towards (but do not reach) a steady state with increasing D. The UM55 profiles change with D more quickly and reach an approximate steady by the $10 - 20$ km profile. The UKV vertical mixing is less efficient than in the UM55 (as discussed in Sect. 3.3) so the profiles take longer to adjust. Unlike the UM55 puff-release passive

scalar profiles (see Fig. 7c), due to the continuous ground-source emissions of passive scalar, there is never more UM55 passive scalar in the upper CBL than the lower CBL (Fig. 9a). However, the ballistic regime turbulent mixing is still occurring as will be explained.

The influence of resolving ballistic dispersion on near-surface concentration is investigated. Figure 9b shows $(\langle c_{0.02}\rangle/c_{BL})_{UM55}/(\langle c_{0.02}\rangle/c_{BL})_{UKV}$, the ratio of the UM55 to UKV $\langle c\rangle/c_{BL}$ at $z/\langle z_i\rangle = 0.02$ at 13:00 UTC. The ratio is calculated in analysis region 2 at 0.5 km intervals downstream of the southern edge of the source. At $D = 1$ km, the proportion of passive scalar at the surface in the UM55 is $\approx 20\%$ lower than in the UKV. This is likely a consequence of differences in vertical grid resolution near the surface. By $D = 8$ km the ratio has decreased from ≈ 0.8 to ≈ 0.53. Using an average CBL advection speed of $U \approx 6$ m s^{-1} (Fig. 2c), this corresponds to air that has been travelling ≈ 22 min since crossing the southern edge of the continuous source region. For the UM55, this agrees well with $\tau_\Omega/2$ (Table 3) and the time at which there are the largest amounts of passive scalar lofted in the CBL in Fig. 7c. This is consistent with the UM55 resolving ballistic dispersion, causing the UM55 to have lower near-surface concentration compared to the UKV at $D \approx 8$ km.

For $D > 8$ km the proportion of passive scalar at the surface in the UM55 relative to the UKV starts to increase again. Although the emission of passive scalar and ballistic mixing at short times continues downstream, the proportion of passive scalar that has had long enough to become well-mixed increases.

By explicitly resolving rather than parameterising vertical mixing within the CBL, up to 34% ($100\times(0.53-0.80)/0.80$) decreases in near-surface concentration can be expected. If the parameterised vertical mixing efficiency in the UKV were increased, it is possible that $(\langle c_{0.02}\rangle/c_{BL})_{UM55}/(\langle c_{0.02}\rangle/c_{BL})_{UKV}$ would be closer to 1, since the parameterised near-surface concentrations would be lower. However, the minimum in $(\langle c_{0.02}\rangle/c_{BL})_{UM55}/(\langle c_{0.02}\rangle/c_{BL})_{UKV}$ at $D \approx U\tau_\Omega/2$ would still occur. K-theory vertical mixing parameterisation used in many NWP and AQM schemes (Kukkonen et al., 2012) cannot produce the elevated concentrations in the upper CBL, since quantities cannot be transported against their local vertical gradient. "Counter-gradient" schemes, which are examples of "non-local" vertical-mixing parametrisations, aim to represent the BL scale coherent convective motions that lead to the "lift-off" behaviour. The lift-off behaviour (where passive scalar is preferentially transported to the upper BL) is a consequence of passive scalar transport by coherent motions at short times since release (i.e., the $t \ll \tau$ ballistic dispersion limit). Simple gamma type counter-gradient parameterisations (i.e., those with similar form to the second term on the right-hand side of Eq. 2) (Deardorff, 1972a; Lock et al., 2016) do not move quantities preferentially from the ground to the upper (rather than the lower) CBL. It is possible that TKE (Mellor and Yamada, 1982; Ito et al., 2015) or eddy-diffusion mass-flux (Siebesma et al., 2007; Pergaud et al., 2009) CBL turbulence schemes could represent this ballistic dispersion behaviour, but to the authors' best knowledge whether they do so accurately has not been investigated.

Lift-off behaviour can be expected to have the largest influence on near-surface air pollution concentration when there is a low proportion of well-mixed pollution. For example, when there is low background pollution concentration (i.e., little long range transported pollution) and at short distances downstream ($D \approx Ut_\Omega/2$) of a strong source. The lifetime of individual pollutant species can also be expected to have an effect.

4 | CONCLUSIONS

CBL dispersion of passive scalar from a homogeneous city-scale ground source is simulated using hectometre and kilometre scale horizontal grid length NWP. We explain the differences in vertical mixing between these scales, develop a reduced analytical model to quantify differences in vertical mixing efficiency, and demonstrate that for certain conditions resolving "ballistic" type dispersion can have a leading order effect on city-scale near-surface pollution

concentration. The case study (4th May 2016) is centred on London, and has clear-sky conditions, with simulated $\langle z_i \rangle = 1.4 - 1.6$ km (11:00-14:00 UTC) and $-\langle z_i \rangle / L_O \approx 30$.

CBL turbulent mixing of scalar in the UKV ($\Delta = O(1\text{km})$) is sub-grid and therefore parameterised, so the passive scalar field varies smoothly in the horizontal. However, in the UM100 and UM55 ($\Delta = O(100\text{m})$) the majority of CBL vertical turbulent mixing is resolved above the surface layer. Passive scalar converges near the surface and ascends in updrafts, before spreading horizontally at the capping inversion. This results in large passive scalar horizontal heterogeneity (e.g., for the continuous release source 2.6% of values are $> 1.64\langle c \rangle$ at $z/\langle z_i \rangle = 0.1$ (Sect. 3.1.2)).

The vertical mixing of passive scalar in the UKV is parameterised using K-theory where movement of particles follows local concentration gradients (i.e., "diffusive" dispersion). For the hour following puff (i.e., instantaneous) release of passive scalar at the ground, this means that the concentration monotonically decreases and increases in the lower and upper CBL, respectively. However, in the UM100 and UM55 where CBL scale overturning eddies are resolved, particles undergo ballistic as well as diffusive dispersion. For times on the order of the turbulence memory timescale, particles retain memory of the eddy they are released into. The largest eddies transport particles into the upper CBL, preferentially over the lower CBL. This "lift-off" behaviour for times $O(\tau_\Omega/2 \sim 20 \text{ min})$ results in higher concentration in the upper than lower BL. To the best of our knowledge, this is the first time lift-off behaviour has been demonstrated using NWP.

Starting from Langevin's equation, a reduced analytical model that takes the form of a damped simple harmonic oscillator is developed. It predicts the CoM trajectory of the puff released passive scalar. The CoM increases ever more slowly with time from the ground towards $z/\langle z_i \rangle = 0.5$ for the UKV, but the CoM overshoots $z/\langle z_i \rangle = 0.5$ (due to the ballistic dispersion) before tending towards $z/\langle z_i \rangle = 0.5$ for the UM100 and UM55. This dispersion behaviour is captured by the overdamped (UKV) and underdamped (UM100/UM55) solutions with remarkable accuracy for such a simple model. The overdamped and underdamped solutions each have two timescales. The UKV has two e-folding timescales, one longer (33.6 min) than the other (8.4 min), explaining why the vertical mixing is efficient initially, but becomes less efficient with time. The UM100 and UM55 have one e-folding timescale (≈ 10 min) that is much shorter than the longer UKV timescale, which explains why at very short times ($0 - 5$ min) their vertical mixing is less efficient than the UKV, but for greater times their vertical mixing is approximately three times more efficient. The other vertical mixing timescale for the UM100 and UM55 is ≈ 40 min, and represents the frequency of the CoM oscillations. With increasing time the vertical concentration gradient reduces in all models, which makes the UKV less efficient at vertical mixing, but the UM100 and UM55 keep mixing efficiently due to the resolved (often counter concentration gradient) CBL overturning eddy transport.

Qualitatively from horizontal (Fig. 4) and vertical (Fig. 3) cross-sections it is seen that more fine-detail structure in both the vertical velocity and passive scalar concentration fields is resolved in the UM55 than the UM100. Using two-point cross-correlation functions (Fig. 5) it is demonstrated that near the top of the surface layer ($z/\langle z_i \rangle = 0.1$) the integral scale turbulence is slightly larger in the UM100 than UM55. However, at $z/\langle z_i \rangle = 0.5$ the integral scale turbulence has similar size in the UM100 and UM55, suggesting that in the middle of the mixed layer the integral scale turbulence has converged or is close to converging with Δ. That the integral scale turbulence in the UM100 and UM55 is similarly well resolved in the mixed layer, is consistent with the UM100 and UM55 having qualitatively similar dispersion behaviour (e.g., Figs. 2a,c, 7, 8) and similar vertical mixing timescales (Table 3).

For an idealised source representing city-scale pollution emissions, it is demonstrated that representing the ballistic type dispersion reduces near-surface passive scalar concentration by up to 34%. At $\sim U \times \tau_\Omega/2 = 8$ km downstream of the (50×50 km) sources' upstream edge, the emissions occurring near the upstream edge have had time to be lifted into the upper CBL, and thus for a reduction in near-surface concentration to develop. This lift-off behaviour can be expected to have its greatest influence on near-surface air pollution concentration when contributions to the

concentration are dominated by local emissions (e.g., for strong city emissions with low concentration air transported in by mesoscale / synoptic scale flow).

Given that the turbulent structure of the CBL is influenced by the amount of surface sensible heating and wind shear, it would be worth investigating other atmospheric conditions, to find out whether the NWP dispersion behaviour exhibited here holds more generally. For example, does the UM100 still behave similarly to the UM55 for less convective conditions and during the morning neutral/convective transition, when z_i and the turbulence integral scale are smaller? Also, more realistic scenarios that include chemistry and heterogeneous pollution sources could be investigated, to see if the ballistic type dispersion still has a large influence on near-surface concentrations. There is evidence that the roughness of the urban surface makes horizontal convective rolls more likely than over rural areas (Miao and Chen, 2008), and that anthropogenic heat emissions in cities can cause weakly convective conditions to occur more often at night (Chapter 7, Oke et al., 2017). Therefore, the extent to which the urban increment changes resolved passive scalar dispersion is of interest. The MetUM does not have a counter-gradient vertical mixing term for passive scalars. Inclusion of such a term would likely increase parametrised CBL vertical mixing efficiency, so that the UKV and UM100/UM55 vertical mixing efficiencies become more similar. However, current counter-gradient parameterisations used in NWP (e.g., Pleim and Chang, 1992; Lock et al., 2000) do not preferentially move passive scalar to the upper (over the lower) CBL, so do not fully represent the dispersion behaviour caused by ballistic dispersion. Assuming that representation of ballistic type dispersion is important for predicting surface-level concentrations in general, new CBL vertical mixing parameterisations (e.g., based on fractional calculus (Paradisi et al., 2001)) should be developed for NWP.

acknowledgements

Appendix 1 – Reduction of the Generalised Langevin Equation to a Damped Simple Harmonic Oscillator

In this section, the generalised Langevin equation (Thomson and Wilson, 2012) is reduced to a damped simple harmonic oscillator (DSHO) describing the CoM evolution of particles puff released at some height in the CBL. In Sect. 3.3 the DSHO is solved and used to estimate vertical mixing timescales for the UKV, UM100, and UM55.

Lagrangian stochastic models (LSMs) are able to produce the correct dispersion behaviour in the diffusive and ballistic limits. The generalised Langevin equation is the usual starting point for modern LSMs, and for vertical dispersion is given by (Thomson, 1987)

$$dw = a(z, w, t)dt + b(z, w, t)d\xi, \tag{11}$$

where $d\xi$ are random velocity increments, and a and b are functions that need to be parameterised. Once w (the vertical velocity of the particle) has been determined one can integrate $dz = w\,dt$ to find the particle position.

The second term on the right-hand side of Eq. 11 is the diffusion term and represents the small scale turbulent motions. Thomson (1987) showed that the random velocity increments must be Gaussian if w is to evolve continuously

in time without jumps. More specifically, $d\xi$ becomes a Gaussian random forcing with zero mean and variance dt. b is generally taken to be

$$b = (C_0 \epsilon)^{1/2}, \tag{12}$$

so that it is consistent with the Lagrangian structure function in the inertial subrange (Weil, 1990). C_0 is often treated as a dispersion parameter but more strictly is a universal constant (Monin and Yaglom (1975), p.358) and ϵ is the local ensemble averaged dissipation rate (Weil, 1990). It is common to express b in terms of the decorrelation timescale $\tau = 2\sigma_w^2/(C_0\epsilon)$ so that $b = (2\sigma_w^2/\tau)^{1/2}$ (Tennekes, 1979; Thomson and Wilson, 2012).

It is well known in CBLs that vertical velocity probability density functions (PDFs) are positively skewed (Weil, 1990). However, to obtain a reduced analytical model we assume Gaussian vertical velocity PDFs throughout the CBL, and note that asymmetries between updrafts and downdrafts, and between the lower and upper BL will not be represented. For stationary, horizontally homogeneous flows, with Gaussian vertical velocity PDF (Thomson, 1987; Weil, 1990)

$$a = -\frac{C_0 \epsilon w}{2\sigma_w^2} + \frac{1}{2}\left(1 + \frac{w^2}{\sigma_w^2}\right)\frac{\partial \sigma_w^2}{\partial z}. \tag{13}$$

The first term on the right-hand side of Eq. 13 is the damping term and represents the fading memory of the turbulence. This can be seen by writing it in terms of the decorrelation timescale so that it equals $-w/\tau$. The second term on the right-hand side of Eq. 13 is the so called drift term and offsets the tendency of simulated particles to accumulate in areas of low σ_w.

Let us take Eqs. 11-13 as the starting point for the reduced analytical model. Except near the ground and the top of the CBL, the ensemble average of the second term on the right-hand side of Eq. 11 is zero, since the Gaussian forcing has equal probability of displacing particles upwards and downwards. This term shall be neglected. The drift term simplifies upon ensemble averaging so that Eqs. 11-13 can be written as

$$\tilde{\tilde{z}} = -\frac{\tilde{z}}{\tau} + \frac{\partial \sigma_w^2}{\partial z}, \tag{14}$$

where $\tilde{z}$ is the ensemble average particle position (or CoM of the particles). We assume that τ is constant which is likely a poorer assumption near the ground and top of the CBL where turbulence characteristics are most different compared to the rest of the CBL.

Turbulence is not vertically homogeneous in the CBL, otherwise the drift term in Eq. 14 would be zero and the characteristic lift-off behaviour of puff released passive scalars near the surface would not be reproduced (Luhar and Britter, 1989; Weil, 1990). Passive scalar would not spread faster than $\langle z^2 \rangle \propto t$ at times shortly after release. For a CBL, the damping and drift terms on the right-hand side of Eq. 14 are of the same order of magnitude, so both should be represented. Here a heuristic approximation is made to the drift term, allowing some representation of the vertical heterogeneity in CBL turbulence, even though it is neglected in the damping term and diffusion term (second term on the right-hand side of Eq. 11). In CBL turbulence σ_w^2 tends to have a maximum at approximately $\langle z_i \rangle/2$ (Salesky et al., 2017). The drift term is therefore positive and negative in the bottom and top halves of the CBL, respectively, and acts to move particles towards $\langle z_i \rangle/2$. It is as if the drift term is a restoring force. On this basis the drift term will be represented as being proportional to the negative displacement from the middle of the CBL.

Another argument for representing the drift term as a restoring force can be made. The main energy producing eddies under convective conditions span the entire CBL depth, and might roughly be approximated as circular in an

$x - z$ plane. A particle released into such an eddy (in the absence of the influence of other eddies) would undergo perpetual circular motions with angular frequency ω analogous to simple harmonic motion when projected onto the z axis.

The LSM has been reduced to a damped simple harmonic oscillator (DSHO) of the form

$$\ddot{\bar{z}} = -2\gamma\dot{\bar{z}} - \omega^2(\bar{z} - \langle z_i \rangle/2), \tag{15}$$

where $\omega = 2\pi/\tau_\omega$ is the natural frequency, τ_ω is expected to be of the order of the eddy turnover timescale, and $\gamma = 1/(2\tau)$ determines the amount of damping. The first and second terms on the right-hand side are the damping and restoring forces, respectively. The $-\langle z_i \rangle/2$ factor places the DSHO equilibrium at the middle of the BL. Note that the time derivative and ensemble average operator orders have been swapped from Eq. 14, assuming that they commute at least to a reasonable approximation.

references

Baklanov, A., Schlünzen, K., Suppan, P., Baldasano, J., Brunner, D., Aksoyoglu, S., Carmichael, G., Douros, J., Flemming, J., Forkel, R. et al. (2014) Online coupled regional meteorology chemistry models in europe: current status and prospects. *Atmospheric Chemistry and Physics*, **14**, 317–398.

Belair, S., Leroyer, S., Seino, N., Spacek, L., Souvanlassy, V. and Paquin-Ricard, D. (2018) Role and impact of the urban environment in a numerical forecast of an intense summertime precipitation event over Tokyo. *Journal of the Meteorological Society of Japan. Ser. II*, **96A**, 77–94.

Best, M., Pryor, M., Clark, D., Rooney, G., Essery, R., Ménard, C., Edwards, J., Hendry, M., Porson, A., Gedney, N. et al. (2011) The Joint UK Land Environment Simulator (JULES), model description–Part 1: energy and water fluxes. *Geoscientific Model Development*, **4**, 677–699.

Blunn, L. P. (2021) *Characterising mixing and pollution transport in the urban boundary layer*. Ph.D. thesis, University of Reading.

Bohnenstengel, S., Evans, S., Clark, P. A. and Belcher, S. (2011) Simulations of the London urban heat island. *Quarterly Journal of the Royal Meteorological Society*, **137**, 1625–1640.

Boutle, I., Eyre, J. and Lock, A. (2014) Seamless stratocumulus simulation across the turbulent gray zone. *Monthly Weather Review*, **142**, 1655–1668.

Boutle, I., Finnenkoetter, A., Lock, A. and Wells, H. (2016) The London Model: forecasting fog at 333 m resolution. *Quarterly Journal of the Royal Meteorological Society*, **142**, 360–371.

Cimorelli, A. J., Perry, S. G., Venkatram, A., Weil, J. C., Paine, R. J., Wilson, R. B., Lee, R. F., Peters, W. D. and Brode, R. W. (2005) AERMOD: A dispersion model for industrial source applications. Part I: General model formulation and boundary layer characterization. *Journal of Applied Meteorology*, **44**, 682–693.

Clark, D., Mercado, L., Sitch, S., Jones, C., Gedney, N., Best, M., Pryor, M., Rooney, G., Essery, R., Blyth, E. et al. (2011) The Joint UK Land Environment Simulator (JULES), model description–Part 2: carbon fluxes and vegetation dynamics. *Geoscientific Model Development*, **4**, 701–722.

Crawford, B., Grimmond, C. S. B., Ward, H. C., Morrison, W. and Kotthaus, S. (2017) Spatial and temporal patterns of surface–atmosphere energy exchange in a dense urban environment using scintillometry. *Quarterly Journal of the Royal Meteorological Society*, **143**, 817–833.

Davies, T., Cullen, M. J., Malcolm, A. J., Mawson, M., Staniforth, A., White, A. and Wood, N. (2005) A new dynamical core for the Met Office's global and regional modelling of the atmosphere. *Quarterly Journal of the Royal Meteorological Society*, **131**, 1759–1782.

Deardorff, J. (1972a) Theoretical expression for the countergradient vertical heat flux. *Journal of Geophysical Research*, **77**, 5900–5904.

Deardorff, J. W. (1970) Preliminary results from numerical integrations of the unstable planetary boundary layer. *Journal of the Atmospheric Sciences*, **27**, 1211–1213.

— (1972b) Numerical investigation of neutral and unstable planetary boundary layers. *Journal of the Atmospheric Sciences*, **29**, 91–115.

Dosio, A., Vilà-Guerau de Arellano, J., Holtslag, A. A. and Builtjes, P. J. (2003) Dispersion of a passive tracer in buoyancy-and shear-driven boundary layers. *Journal of Applied Meteorology*, **42**, 1116–1130.

Dosio, A., Guerau de Arellano, J. V., Holtslag, A. A. and Builtjes, P. J. (2005) Relating Eulerian and Lagrangian statistics for the turbulent dispersion in the atmospheric convective boundary layer. *Journal of the Atmospheric Sciences*, **62**, 1175–1191.

Garratt, J. (1994) *The Atmospheric Boundary Layer*. Cambridge University Press.

Gopalakrishnan, S. and Avissar, R. (2000) An LES study of the impacts of land surface heterogeneity on dispersion in the convective boundary layer. *Journal of the Atmospheric Sciences*, **57**, 352–371.

Hagelin, S., Auger, L., Brovelli, P. and Dupont, O. (2014) Nowcasting with the AROME model: first results from the high-resolution AROME airport. *Weather and forecasting*, **29**, 773–787.

Halliwell, C. (2017) Subgrid turbulence scheme. Unified Model Documentation Paper 28, Met Office.

Hanley, K. E., Barrett, A. I. and Lean, H. W. (2016) Simulating the 20 May 2013 Moore, Oklahoma tornado with a 100-metre grid-length NWP model. *Atmospheric Science Letters*, **17**, 453–461.

Hanley, K. E., Plant, R. S., Stein, T. H., Hogan, R. J., Nicol, J. C., Lean, H. W., Halliwell, C. and Clark, P. A. (2015) Mixing-length controls on high-resolution simulations of convective storms. *Quarterly Journal of the Royal Meteorological Society*, **141**, 272–284.

Honnert, R., Efstathiou, G. A., Beare, R. J., Ito, J., Lock, A., Neggers, R., Plant, R. S., Shin, H. H., Tomassini, L. and Zhou, B. (2020) The Atmospheric Boundary Layer and the "Gray Zone" of Turbulence: A critical review. *Journal of Geophysical Research: Atmospheres*, e2019JD030317.

Honnert, R., Masson, V. and Couvreux, F. (2011) A diagnostic for evaluating the representation of turbulence in atmospheric models at the kilometric scale. *Journal of the Atmospheric Sciences*, **68**, 3112–3131.

Ito, J., Niino, H., Nakanishi, M. and Moeng, C.-H. (2015) An extension of the Mellor–Yamada model to the terra incognita zone for dry convective mixed layers in the free convection regime. *Boundary-layer meteorology*, **157**, 23–43.

Kotthaus, S. and Grimmond, C. S. B. (2014) Energy exchange in a dense urban environment–part 1: Temporal variability of long-term observations in central london. *Urban Climate*, **10**, 261–280.

Kukkonen, J., Olsson, T., Schultz, D. M., Baklanov, A., Klein, T., Miranda, A. I., Monteiro, A., Hirtl, M., Tarvainen, V., Boy, M., Peuch, V.-H., Poupkou, A., Kioutsioukis, I., Finardi, S., Sofiev, M., Sokhi, R., Lehtinen, K. E. J., Karatzas, K., San José, R., Astitha, M., Kallos, G., Schaap, M., Reimer, E., Jakobs, H. and Eben, K. (2012) A review of operational, regional-scale, chemical weather forecasting models in Europe. *Atmospheric Chemistry and Physics*, **12**, 1–87.

Lean, H. W., Barlow, J. F. and Clark, P. A. (2022) The use of 100 m scale nwp models to understand differences between different measures of mixing height in a morning growing clear convective boundary layer over london. *Quarterly Journal of the Royal Meteorological Society*, **148**, 1983–1995.

Lean, H. W., Barlow, J. F. and Halios, C. H. (2019) The impact of spin-up and resolution on the representation of a clear convective boundary layer over London in order 100 m grid-length versions of the Met Office Unified Model. *Quarterly Journal of the Royal Meteorological Society*, **145**, 1674–1689.

Leroyer, S., Bélair, S., Husain, S. Z. and Mailhot, J. (2014) Subkilometer numerical weather prediction in an urban coastal area: A case study over the Vancouver metropolitan area. *Journal of Applied Meteorology and Climatology*, **53**, 1433–1453.

Leroyer, S., Bélair, S., Souvanlasy, V., Vallée, M., Pellerin, S. and Sills, D. (2022) Summertime assessment of an urban-scale numerical weather prediction system for Toronto. *Atmosphere*, **13**, 1030.

Lilly, D. K. (1962) On the numerical simulation of buoyant convection. *Tellus*, **14**, 148–172.

— (1968) Models of cloud-topped mixed layers under a strong inversion. *Quarterly Journal of the Royal Meteorological Society*, **94**, 292–309.

Lock, A., Brown, A., Bush, M., Martin, G. and Smith, R. (2000) A new boundary layer mixing scheme. Part I: Scheme description and single-column model tests. *Monthly Weather Review*, **128**, 3187–3199.

Lock, A., Edwards, J. and Boutle, I. (2016) The parametrization of boundary layer processes. Unified Model Documentation Paper 24, Met Office.

Luhar, A. K. and Britter, R. E. (1989) A random walk model for dispersion in inhomogeneous turbulence in a convective boundary layer. *Atmospheric Environment*, **23**, 1911–1924.

McHugh, C., Carruthers, D. and Edmunds, H. (1997) ADMS-urban: an air quality management system for traffic, domestic and industrial pollution. *International Journal of Environment and Pollution*, **8**, 666–674.

Mellor, G. L. and Yamada, T. (1982) Development of a turbulence closure model for geophysical fluid problems. *Reviews of Geophysics*, **20**, 851–875.

Miao, S. and Chen, F. (2008) Formation of horizontal convective rolls in urban areas. *Atmospheric Research*, **89**, 298–304.

Monin, A. and Yaglom, A. (1975) *Statistical fluid mechanics: mechanics of turbulence*. MIT Press.

Oke, T. R., Mills, G. and Voogt, J. (2017) *Urban climates*. Cambridge University Press.

Paradisi, P., Cesari, R., Mainardi, F., Maurizi, A. and Tampieri, F. (2001) A generalized Fick's law to describe non-local transport effects. *Physics and Chemistry of the Earth, Part B: Hydrology, Oceans and Atmosphere*, **26**, 275–279.

Pergaud, J., Masson, V., Malardel, S. and Couvreux, F. (2009) A parameterization of dry thermals and shallow cumuli for mesoscale numerical weather prediction. *Boundary-layer meteorology*, **132**, 83–106.

Pleim, J. E. (2007) A combined local and nonlocal closure model for the atmospheric boundary layer. Part I: Model description and testing. *Journal of Applied Meteorology and Climatology*, **46**, 1383–1395.

Pleim, J. E. and Chang, J. S. (1992) A non-local closure model for vertical mixing in the convective boundary layer. *Atmospheric Environment. Part A. General Topics*, **26**, 965–981.

Porson, A., Clark, P. A., Harman, I., Best, M. and Belcher, S. (2010) Implementation of a new urban energy budget scheme in the MetUM. Part I: Description and idealized simulations. *Quarterly Journal of the Royal Meteorological Society*, **136**, 1514–1529.

Ronda, R., Steeneveld, G., Heusinkveld, B., Attema, J. and Holtslag, A. (2017) Urban finescale forecasting reveals weather conditions with unprecedented detail. *Bulletin of the American Meteorological Society*, **98**, 2675–2688.

Salesky, S. T., Chamecki, M. and Bou-Zeid, E. (2017) On the nature of the transition between roll and cellular organization in the convective boundary layer. *Boundary-Layer Meteorology*, **163**, 41–68.

Schmidt, H. and Schumann, U. (1989) Coherent structure of the convective boundary layer derived from large-eddy simulations. *Journal of Fluid Mechanics*, **200**, 511–562.

Siebesma, A. P., Soares, P. M. and Teixeira, J. (2007) A combined eddy-diffusivity mass-flux approach for the convective boundary layer. *Journal of the atmospheric sciences*, **64**, 1230–1248.

Smagorinsky, J. (1963) General circulation experiments with the primitive equations: 1. The basic experiment. *Monthly Weather Review*, **91**, 99–164.

Stockie, J. M. (2011) The mathematics of atmospheric dispersion modeling. *SIAM Review*, **53**, 349–372.

Tang, Y., Lean, H. W. and Bornemann, J. (2013) The benefits of the Met Office variable resolution NWP model for forecasting convection. *Meteorological Applications*, **20**, 417–426.

Taylor, G. I. (1922) Diffusion by continuous movements. *Proceedings of the London Mathematical Society*, **2**, 196–212.

Tennekes, H. (1979) The exponential lagrangian correlation function and turbulent diffusion in the inertial subrange. *Atmospheric Environment*, **13**, 1565–1567.

Thomson, D. (1987) Criteria for the selection of stochastic models of particle trajectories in turbulent flows. *Journal of Fluid Mechanics*, **180**, 529–556.

Thomson, D. and Wilson, J. (2012) History of Lagrangian stochastic models for turbulent dispersion. *Lagrangian Modeling of the Atmosphere*, **200**, 19–36.

Warhaft, Z. (2000) Passive scalars in turbulent flows. *Annual Review of Fluid Mechanics*, **32**, 203–240.

Webster, H. and Thomson, D. (2018) NAME – Model Description. User Guide for NAME, UK Met Office.

Weil, J. (1990) A diagnosis of the asymmetry in top-down and bottom-up diffusion using a Lagrangian stochastic model. *Journal of the Atmospheric Sciences*, **47**, 501–515.

Willis, G. and Deardorff, J. (1976) A laboratory model of diffusion into the convective planetary boundary layer. *Quarterly Journal of the Royal Meteorological Society*, **102**, 427–445.

— (1979) Laboratory observations of turbulent penetrative-convection planforms. *Journal of Geophysical Research: Oceans*, **84**, 295–302.

Willis, G. E. and Deardorff, J. W. (1981) A laboratory study of dispersion from a source in the middle of the convectively mixed layer. *Atmospheric Environment*, **15**, 109–117.

Wilson, J. D. and Sawford, B. L. (1996) Review of lagrangian stochastic models for trajectories in the turbulent atmosphere. *Boundary-Layer Meteorology*, **78**, 191–210.

Wood, N., Staniforth, A., White, A., Allen, T., Diamantakis, M., Gross, M., Melvin, T., Smith, C., Vosper, S., Zerroukat, M. et al. (2014) An inherently mass-conserving semi-implicit semi-Lagrangian discretization of the deep-atmosphere global non-hydrostatic equations. *Quarterly Journal of the Royal Meteorological Society*, **140**, 1505–1520.

Wyngaard, J. C. (2004) Toward numerical modeling in the "Terra Incognita". *Journal of the Atmospheric Sciences*, **61**, 1816–1826.

Wyngaard, J. C. and Brost, R. A. (1984) Top-down and bottom-up diffusion of a scalar in the convective boundary layer. *Journal of the Atmospheric Sciences*, **41**, 102–112.

1
2
3
4
5
6
7
8
9
10
11
12
13
14
15
16
17
18
19
20
21
22
23
24
25
26
27
28
29
30
31
32
33
34
35
36
37
38
39
40
41
42
43
44
45
46
47
48
49
50
51
52
53
54
55
56
57
58
59
60

The influence of resolved convective motions on scalar dispersion in hectometric scale numerical weather prediction models

Lewis P. Blunn | Robert S. Plant* | Omduth Coceal | Sylvia I. Bohnenstengel | Humphrey W. Lean | Janet F. Barlow

c/c_{BL}
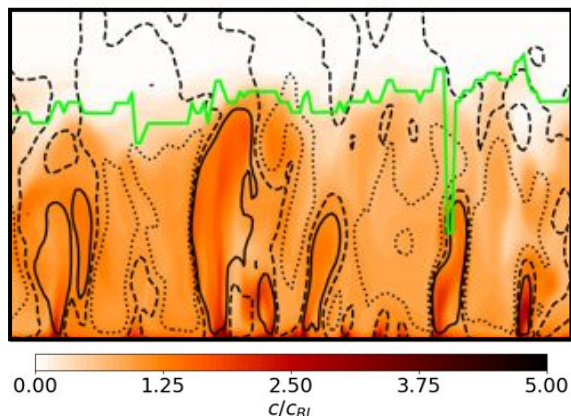
In the not-too-distant future it will be possible to routinely run weather and air quality models at sub-km grid lengths. At such grid lengths convective boundary layer motions start to become resolved. In this article, we demonstrate that this will have significant implications for vertical mixing and city-scale transport of pollution emissions. A key reason is the ability of the higher-resolution runs to capture the ballistic dispersion regime, which results in a two-timescale behaviour.